

This is the accepted manuscript made available via CHORUS, the article has been published as:

# Multiphoton above-threshold ionization in superintense free-electron x-ray laser fields: Beyond the dipole approximation

Zhongyuan Zhou and Shih-I Chu

Phys. Rev. A **87**, 023407 — Published 13 February 2013

DOI: [10.1103/PhysRevA.87.023407](https://doi.org/10.1103/PhysRevA.87.023407)

# Multiphoton Above-Threshold Ionization in Superintense Free Electron X-Ray Laser Fields: Beyond the Dipole Approximation

Zhongyuan Zhou<sup>1,2\*</sup> and Shih-I Chu<sup>1,3†</sup>

<sup>1</sup>*Department of Chemistry, University of Kansas, Lawrence, KS 66045 USA*

<sup>2</sup>*Department of Physics and Astronomy, University of Georgia, Athens, Georgia 30602 USA*

<sup>3</sup>*Center for Quantum Science and Engineering, Department of Physics,  
National Taiwan University, Taipei 10617, Taiwan*

(Dated: January 29, 2013)

We present an accurate and efficient nondipole computational approach in momentum space for the nonperturbative study of multiphoton above-threshold ionization (ATI) of atoms in superintense and ultrashort-wavelength laser fields. This approach has been successfully used to investigate the multiphoton processes of a hydrogen atom exposed to superintense free electron X-ray laser fields. We find that compared to dipole approximation the nondipole ATI spectra are enhanced substantially in high energy regime and the photoelectron angular distributions (PADs) are distorted significantly in higher-intensity and/or longer-pulse laser fields, in particular two lobes are induced along and against the laser propagation direction. The origin of these phenomena has been explored in details.

PACS numbers: 32.80.Rm, 32.80.Fb, 33.80.Rv

## I. INTRODUCTION

With the recent development of free electron lasers (FELs), particularly the “fourth generation” accelerator-based FELs [1–3], the study of multiphoton processes of atoms and molecules in superintense ultrashort-wavelength and X-ray laser fields attracts more and more attention [4–9]. Theoretical investigation of the multiphoton processes in superintense and ultrashort-wavelength laser fields may encounter twofold difficulties. (1) In superintense laser fields, an electron can achieve extremely high energy and go to the place very far from the nucleus. To accurately calculate the wavefunction of the electron in spatial coordinate ( $\mathcal{R}$ ) space, the boundary has to be set at very large distance from the nucleus to avoid reflection. This requires the use of a very large number of grid points and thus makes the calculation difficult. (2) In superintense and ultrashort-wavelength laser fields, owing to the ionization of electron the characteristic spatial scale of the system may be comparable to or even larger than the laser wavelength and the spatial dependence of the laser fields may not be neglected. In this case, the dipole approximation is no longer a good approach, instead the nondipole approach that includes nondipole interactions is desirable. Due to the spatial dependence, a fully three-dimensional (3D) calculation is essential in the nondipole approach even for hydrogen-like atoms. Thus a huge number of grid points are necessary in the nondipole calculation, which is still a great challenge to current available supercomputers.

To conquer the first difficulty, an efficient dipole computational approach has been proposed recently in momentum ( $\mathcal{P}$ ) space [10]. This approach is based on the fact that the momentum of an electron is always finite and less than a certain maximum value  $k_M$ , and the probability of electron is negligible when the electron momentum is greater than  $k_M$ . Thus the wavefunction of electron can be calculated within a finite  $\mathcal{P}$  space with a simple zero boundary condition as long as the boundary is set at a properly large  $k_M$ . This approximation has been successfully used to study the multiphoton above-threshold ionization (ATI) spectra of a hydrogen atom in longer-wavelength and shorter-pulse laser fields where the nondipole interactions can be ignored.

To vanquish the second difficulty, an  $\mathcal{R}$ -space nondipole approach has been proposed within the Kramers-Henneberger frame by neglecting some higher-order nondipole interactions [11, 12]. This approach has been used to study multiphoton ionization processes of a hydrogen atom interacting with XUV laser fields [11, 12]. It is shown that the photoelectron angular distributions (PADs) are quite different from those of dipole approximation when the pulse durations are larger than 5 optical cycles (OCs) for the laser fields with the field strength of 30 a.u. [12]. Particularly an extra lobe is induced against the laser propagation direction. However, the multiphoton ATI spectra do not have obvious difference from the dipole ones for the laser pulses with the duration of 5 OCs [11]. This approach

---

\*Electronic address: zyzhou@uga.edu

†Electronic address: sichu@ku.edu

has also been used to investigate the multiphoton ionization processes of a hydrogen atom in excited states [13] and a hydrogen molecular ion  $\text{H}_2^+$  [14]. The predicted PADs for these processes have multilobe structures.

In this paper, we propose a  $\mathcal{P}$ -space nondipole computational approach for the study of multiphoton ATI of atoms exposed to superintense ultrashort-wavelength laser fields. This approach includes all the nondipole interactions and has been applied to the calculation of multiphoton ATI spectra and PADs of a hydrogen atom in superintense X-ray (with wavelength  $\lambda = 9.11$  nm) laser fields. It is shown that the ATI spectra are enhanced substantially in the high energy region and the PADs are distorted significantly in the higher-intensity and/or longer-pulse laser fields compared to those of dipole approximation. In particular, two lobes are induced along and against the laser propagation direction, respectively. The physical mechanism for these phenomena is explored.

## II. THEORETICAL METHODOLOGY

### A. Nondipole time-dependent Schrödinger equation

In velocity gauge, the nondipole Hamiltonian of an electron in joint Coulomb and laser fields is given by (atomic units are used throughout this paper unless otherwise indicated)

$$H(\mathbf{r}, t) = \frac{1}{2} \left( \mathbf{p} + \frac{1}{c} \mathbf{A} \right)^2 + V(\mathbf{r}), \quad (1)$$

where,  $\mathbf{p} = -i\nabla$  is the electron momentum operator,  $V(\mathbf{r})$  is the Coulomb potential,  $c$  is the speed of light in vacuum, and  $\mathbf{A}(\mathbf{r}, t)$  is the vector potential of the laser field. For a sine-squared laser pulse linearly polarized in  $x$  axis and propagated along  $z$  axis, the vector potential is

$$\mathbf{A}(\mathbf{r}, t) = \mathbf{e}_x \frac{cE_0}{\omega} \sin^2 \left( \frac{\pi\eta}{\omega T_P} \right) \sin(\eta + \phi), \quad (2)$$

where,  $E_0$  is the laser field strength,  $T_P$  is the pulse duration,  $\phi$  is the carrier-envelope phase (CEP),  $\eta = \omega t - \mathbf{k}_L \cdot \mathbf{r}$ ,  $\mathbf{k}_L = k_L \mathbf{e}_z$ ,  $k_L = 2\pi/\lambda = \omega/c$ ,  $\omega$  is the laser angular frequency,  $\mathbf{e}_x$  is the unit vector of  $x$  axis, and  $\mathbf{e}_z$  is the unit vector of  $z$  axis. For the laser fields considered here, the propagation direction is perpendicular to the polarization direction and thus  $\mathbf{k}_L \perp \mathbf{A}$ . In Coulomb gauge,  $\nabla \cdot \mathbf{A} = 0$  and the nondipole Hamiltonian Eq. (1) is recast to

$$H(\mathbf{r}, t) = \frac{1}{2} \left( \mathbf{p}^2 + \frac{2}{c} \mathbf{A} \cdot \mathbf{p} + \frac{\mathbf{A}^2}{c^2} \right) + V(\mathbf{r}). \quad (3)$$

The  $\mathcal{R}$ -space nondipole time-dependent Schrödinger equation (TDSE) is

$$i \frac{\partial}{\partial t} \Phi(\mathbf{r}, t) = H(\mathbf{r}, t) \Phi(\mathbf{r}, t). \quad (4)$$

The relation between the  $\mathcal{R}$ -space wavefunction  $\Phi(\mathbf{r}, t)$  and  $\mathcal{P}$ -space wavefunction  $\varphi(\mathbf{k}, t)$  is given by Fourier transform

$$\Phi(\mathbf{r}, t) = \frac{1}{(2\pi)^{3/2}} \int \varphi(\mathbf{k}, t) \exp(i\mathbf{k} \cdot \mathbf{r}) d\mathbf{k}. \quad (5)$$

Applying Eqs. (3) and (5) to Eq. (4), multiplying Eq. (4) with  $\exp(-i\mathbf{k} \cdot \mathbf{r})$ , and integrating Eq. (4) over  $\mathbf{r}$ , we obtain the  $\mathcal{P}$ -space nondipole TDSE

$$i \frac{\partial \varphi(\mathbf{k}, t)}{\partial t} = \int H(\mathbf{k}, \mathbf{k}', t) \varphi(\mathbf{k}', t) d\mathbf{k}', \quad (6)$$

with the  $\mathcal{P}$ -space Hamiltonian given by

$$H(\mathbf{k}, \mathbf{k}', t) = \frac{\mathbf{k}^2}{2} \delta(\mathbf{k} - \mathbf{k}') + V(\mathbf{k}, \mathbf{k}') + D(\mathbf{k}, \mathbf{k}', t) + B(\mathbf{k}, \mathbf{k}', t), \quad (7)$$

where,

$$V(\mathbf{k}, \mathbf{k}') = \frac{1}{(2\pi)^3} \int V(\mathbf{r}) \exp[i(\mathbf{k}' - \mathbf{k}) \cdot \mathbf{r}] d\mathbf{r}, \quad (8)$$

$$D(\mathbf{k}, \mathbf{k}', t) = \frac{1}{(2\pi)^3} \int \left[ \frac{1}{2c} \mathbf{A} \cdot (\mathbf{k} + \mathbf{k}') \right] \exp[i(\mathbf{k}' - \mathbf{k}) \cdot \mathbf{r}] d\mathbf{r}, \quad (9)$$

and

$$B(\mathbf{k}, \mathbf{k}', t) = \frac{1}{(2\pi)^3} \int \left( \frac{\mathbf{A}^2}{2c^2} \right) \exp[i(\mathbf{k}' - \mathbf{k}) \cdot \mathbf{r}] d\mathbf{r}, \quad (10)$$

are the  $\mathcal{P}$ -space Coulomb potential and laser-electron interactions, respectively. In general, the  $\mathcal{P}$ -space Coulomb potential is calculated from the  $\mathcal{R}$ -space Coulomb potential via the Fourier transform Eq. (8). For a hydrogen-like atom, the  $\mathcal{P}$ -space Coulomb potential can be calculated analytically. For a hydrogen-like atom with a nuclear charge  $Z$ , the  $\mathcal{P}$ -space Coulomb potential is given by

$$V(\mathbf{k}, \mathbf{k}') = \frac{1}{(2\pi)^3} \int \left( -\frac{Z}{|\mathbf{r}|} \right) \exp[i(\mathbf{k}' - \mathbf{k}) \cdot \mathbf{r}] d\mathbf{r} = -\frac{Z}{2\pi^2} \frac{1}{|\mathbf{k} - \mathbf{k}'|^2}. \quad (11)$$

This potential has a quadratic singularity at  $\mathbf{k} = \mathbf{k}'$  [15, 16]. For an arbitrary one-electron binding potential, the  $\mathcal{P}$ -space counterpart can be computed numerically. Since the binding potential decreases with the radial distance of electron from nucleus the integral in the Fourier transform is integrable and the  $\mathcal{P}$ -space potential can be numerically computed. Because the binding potential is time-independent the  $\mathcal{P}$ -space binding potential is also time-independent and only needs to be calculated once on the  $\mathcal{P}$ -space grid points before the  $\mathcal{P}$ -space wavefunction propagation. For the vector potential given by Eq. (2),  $D(\mathbf{k}, \mathbf{k}', t)$  and  $B(\mathbf{k}, \mathbf{k}', t)$  are calculated by Eqs. (A1) and (A2) in Appendix A, respectively.

### B. Partial wave expansion and radial wavefunction

To calculate the wavefunction, the  $\mathcal{P}$ -space Coulomb potential  $V(\mathbf{k}, \mathbf{k}')$  is expanded, in spherical coordinates, in partial waves as

$$V(\mathbf{k}, \mathbf{k}') = \frac{1}{kk'} \sum_{lm, l'm'} V_l(k, k') Y_{lm}(\theta, \phi) Y_{l'm'}^*(\theta', \phi') \delta_{ll'} \delta_{mm'}, \quad (12)$$

where,  $k = |\mathbf{k}|$ ,  $Y_{lm}(\theta, \phi)$  is the spherical harmonic, and  $V_l(k, k')$  is the partial wave Coulomb potential given by

$$V_l(k, k') = kk' \sum_{l'm'} \int \int Y_{lm}^*(\theta, \phi) V(\mathbf{k}, \mathbf{k}') Y_{l'm'}(\theta', \phi') d\Omega d\Omega'. \quad (13)$$

Here,  $d\Omega = \sin\theta d\theta d\phi$ ,  $l \in [0, L_M]$ ,  $m \in [-l, l]$ , and  $L_M$  is the maximum number of partial waves. For hydrogen-like atoms, the partial wave Coulomb potential is calculated by

$$V_l(k, k') = -\frac{Z}{\pi} Q_l(z), \quad (14)$$

where,  $z = (k^2 + k'^2)/2kk'$  and  $Q_l(z)$  is Legendre function of the second kind [15, 16]. It has a logarithmic singularity at  $k = k'$ .

Similarly, the  $\mathcal{P}$ -space laser-electron interaction terms  $D(\mathbf{k}, \mathbf{k}', t)$  and  $B(\mathbf{k}, \mathbf{k}', t)$  can be expanded in partial waves as

$$D(\mathbf{k}, \mathbf{k}', t) = \frac{1}{kk'} \sum_{lm, l'm'} D_{lm, l'm'}(k, k', t) Y_{lm}(\theta, \phi) Y_{l'm'}^*(\theta', \phi'), \quad (15)$$

and

$$B(\mathbf{k}, \mathbf{k}', t) = \frac{1}{kk'} \sum_{lm, l'm'} B_{lm, l'm'}(k, k', t) Y_{lm}(\theta, \phi) Y_{l'm'}^*(\theta', \phi'), \quad (16)$$

where, the partial wave laser-electron interaction terms  $D_{lm, l'm'}(k, k', t)$  and  $B_{lm, l'm'}(k, k', t)$  can be calculated by

$$D_{lm, l'm'}(k, k', t) = kk' \int \int Y_{lm}^*(\theta, \phi) D(\mathbf{k}, \mathbf{k}', t) Y_{l'm'}(\theta', \phi') d\Omega d\Omega', \quad (17)$$

and

$$B_{lm,l'm'}(k,k',t) = kk' \int \int Y_{lm}^*(\theta, \phi) B(\mathbf{k}, \mathbf{k}', t) Y_{l'm'}(\theta', \phi') d\Omega d\Omega', \quad (18)$$

respectively. For the laser pulse given by Eq. (2),  $D_{lm,l'm'}(k,k',t)$  and  $B_{lm,l'm'}(k,k',t)$  are calculated by Eqs. (B1) and (B2) in Appendix B, respectively.

The wavefunction  $\varphi(\mathbf{k}, t)$  is expanded in partial waves as

$$\varphi(\mathbf{k}, t) = \frac{1}{k} \sum_{lm} R_{lm}(k, t) Y_{lm}(\theta, \phi), \quad (19)$$

where  $R_{lm}(k, t)$  is the  $\mathcal{P}$ -space radial wavefunction.

Substituting Eqs. (7), (12), (15), (16), and (19) into Eq. (6), multiplying Eq. (6) with  $Y_{lm}(\theta, \phi)$ , and integrating Eq. (6) over the angles  $(\theta, \phi)$ , we obtain an integro-differential equation for the  $\mathcal{P}$ -space radial wavefunction  $R_{lm}(k, t)$

$$\begin{aligned} i \frac{\partial R_{lm}(k, t)}{\partial t} &= \frac{k^2}{2} R_{lm}(k, t) + \int V_l(k, k') R_{lm}(k', t) dk' \\ &+ \sum_{l'm'} \int D_{lm,l'm'}(k, k', t) R_{l'm'}(k', t) dk' \\ &+ \sum_{l'm'} \int B_{lm,l'm'}(k, k', t) R_{l'm'}(k', t) dk'. \end{aligned} \quad (20)$$

For longer-wavelength, lower-intensity, and shorter-pulse laser fields,  $\mathbf{k}_L \cdot \mathbf{r} \sim r/\lambda \rightarrow 0$  and the dependence of  $\mathbf{A}$  on spatial coordinates can be neglected. In this case,  $D(\mathbf{k}, \mathbf{k}', t) = \mathbf{A} \cdot \mathbf{k} \delta(\mathbf{k}' - \mathbf{k})/c$  and  $B(\mathbf{k}, \mathbf{k}', t) = \mathbf{A}^2 \delta(\mathbf{k}' - \mathbf{k})/2c^2$ . After substituting Eq. (7) into Eq. (6), the third term on the right-hand side (RHS) of Eq. (6),  $(\mathbf{A} \cdot \mathbf{k}/c) \varphi(\mathbf{k}, t)$ , represents the dipole interaction while the fourth term,  $(\mathbf{A}^2/2c^2) \varphi(\mathbf{k}, t)$ , only changes the phase of the wavefunction and thus can be removed using a transform. In this case, Eq. (6) is degraded to the equation of dipole approximation [10].

### III. NUMERICAL RECIPES

#### A. Landé subtraction technique

To remove the singularity in Coulomb potential, Landé subtraction technique [15, 17] is applied to the calculation of the term containing  $V_l(k, k')$ . Based on this technique, the second term on the RHS of Eq. (20) can be computed by [10]

$$\begin{aligned} &\int V_l(k, k') R_{lm}(k', t) dk' \\ &= k S_l R_{lm}(k, t) + \int V_l(k, k') \left[ R_{lm}(k', t) - \frac{R_{lm}(k, t)}{P_l(z)} \frac{k}{k'} \right] dk', \end{aligned} \quad (21)$$

where,  $P_l(z)$  is Legendre polynomial and  $S_l$  is given by

$$S_l = \int \frac{V_l(k, k')}{P_l(z)} \frac{dk'}{k'}, \quad (22)$$

and can be calculated numerically [18]. Introducing a singularity-free potential

$$v_l(k, k') = \begin{cases} 0, & k' = k \\ V_l(k, k'), & k' \neq k \end{cases}. \quad (23)$$

Substituting Eq. (21) into Eq. (20) and using Eq. (23), we achieve a singularity-free equation for the  $\mathcal{P}$ -space radial wavefunction  $R_{lm}(k, t)$

$$\begin{aligned} i \frac{\partial R_{lm}(k, t)}{\partial t} = & \left[ \frac{k^2}{2} + kS_l - kq_l(k) \right] R_{lm}(k, t) \\ & + \sum_{l'm'} \int v_l(k, k') \delta_{ll'} \delta_{mm'} R_{l'm'}(k', t) dk' \\ & + \sum_{l'm'} \int D_{lm, l'm'}(k, k', t) R_{l'm'}(k', t) dk' \\ & + \sum_{l'm'} \int B_{lm, l'm'}(k, k', t) R_{l'm'}(k', t) dk', \end{aligned} \quad (24)$$

where,

$$q_l(k) = \int \frac{v_l(k, k')}{P_l(z)} \frac{dk'}{k'}. \quad (25)$$

Solving Eq. (24) the  $\mathcal{P}$ -space radial wavefunction is obtained, from which the ATI spectra and PADs are calculated.

### B. $\mathcal{P}$ -space generalized pseudospectral method

To solve Eq. (24), we extend the  $\mathcal{R}$ -space generalized pseudospectral (GPS) method [19, 20] to the  $\mathcal{P}$  space [10]. Since the  $\mathcal{P}$ -space wavefunction can be set to zero on the boundary with the momentum  $k_M$ , we will confine our calculations in the volume of  $k \in [0, k_M]$ . To use the GPS method, the  $\mathcal{P}$ -space domain  $k \in [0, k_M]$  is mapped to a new domain  $x \in [-1, 1]$  by a mapping function

$$k(x) = \gamma \frac{1+x}{1-x+x_M}, \quad (26)$$

where,  $x_M = 2\gamma/k_M$  and  $\gamma$  is a mapping parameter. The smaller the value of  $\gamma$ , the denser the grid points at small momentum  $k$ . By using the mapping function, the grid points can be adjusted flexibly in some range and the calculation is improved. It is shown that for the  $\mathcal{R}$ -space calculations involving Coulomb potentials [19, 20] the eigenvalues and eigenfunctions achieved by using the mapped grid points are more accurate than those of the equal-spacing grid points if the same number of grid points are used in the computation. It is also shown that the GPS method with the mapping function (26) is a very accurate method to the  $\mathcal{P}$ -space calculation [10].

To calculate the radial wavefunction, Eq. (24) is mapped to the domain  $x \in [-1, 1]$  and discretized by using Gaussian quadrature with  $N_M$  grid points. Then a time-dependent (TD) matrix equation is obtained

$$i \frac{\partial y_{jlm}(t)}{\partial t} = \left[ \frac{k_j^2}{2} + k_j S_l - k_j q_{jl} \right] y_{jlm}(t) + \sum_{j'=1}^N u_{jj'}^l y_{j'lm}(t) + \sum_{j'l'm'} f_{jlm, j'l'm'} y_{j'l'm'}(t), \quad (27)$$

with

$$y_{jlm}(t) = \sqrt{\dot{k}_j w_j} R_{jlm}(t), \quad (28)$$

$$u_{jj'}^l = v_{jj'}^l \sqrt{\dot{k}_j w_j \dot{k}_{j'} w_{j'}}, \quad (29)$$

and

$$f_{jlm, j'l'm'} = (D_{jlm, j'l'm'} + B_{jlm, j'l'm'}) \sqrt{\dot{k}_j w_j \dot{k}_{j'} w_{j'}}, \quad (30)$$

where,  $w_j$  is the weight of Gaussian quadrature, subscript  $j$  denotes the  $j$ th grid point,  $k_j = k(x_j)$ ,  $R_{jlm} = R_{lm}(k_j, t)$ ,  $\dot{k}_j = dk/dx|_{x_j}$ ,  $q_{jl} = q_l(k_j)$ ,  $v_{jj'}^l = v_l(k_j, k_{j'})$ ,  $B_{jlm, j'l'm'} = B_{lm, l'm'}(k_j, k_{j'}, t)$ , and  $D_{jlm, j'l'm'} = D_{lm, l'm'}(k_j, k_{j'}, t)$ . From Eqs. (B1) to (B4),  $D_{lm, l'm'}(k, k', t) \neq 0$  when and only when  $m' = m \pm 1$  and  $B_{lm, l'm'}(k, k', t) \neq 0$  when and

only when  $m' = m$ . Thus the matrix element  $f_{jlm,j'l'm'} \neq 0$  when and only when  $m' = m$  or  $m \pm 1$  and the matrix  $\mathbf{F} = \{f_{jlm,j'l'm'}\}$  is sparse.

For convenience, Eq. (27) is rewritten in a matrix form as

$$i \frac{\partial}{\partial t} \mathbf{Y}(t) = [\mathbf{H}_0 + \mathbf{F}(t)] \mathbf{Y}(t), \quad (31)$$

where,  $\mathbf{Y}(t) = \{y_{jlm}(t)\}$ ,  $\mathbf{H}_0 = \{h_{jj'}^l \delta_{ll'} \delta_{mm'}\}$ , and  $\mathbf{F}(t) = \{f_{jlm,j'l'm'}\}$ . Here,  $h_{jj'}^l$  is the unperturbed Hamiltonian matrix element given by

$$h_{jj'}^l = \left( \frac{k_j^2}{2} + k_j S_l - k_j q_{jl} \right) \delta_{jj'} + u_{jj'}^l. \quad (32)$$

### C. Propagation of the wavefunction

Solving the TD matrix equation (31) is a demanding task due to the very large dimension of the matrix equation for superintense laser fields. However, since the matrix  $\mathbf{F}(t)$  is sparse, the Hamiltonian matrix  $\mathbf{H}_0 + \mathbf{F}(t)$  is also sparse. To fully take advantage of the property of the sparse matrix, we employ the symplectic algorithm [21] to propagate the TD matrix equation (31). The symplectic algorithm keeps the norm of wavefunction reserved and allows large time step in the propagation of the wavefunction. One of the frequently used symplectic algorithms is Euler mid-point algorithm. Applying this algorithm to Eq. (31), one has

$$\frac{\mathbf{Y}^{n+1} - \mathbf{Y}^n}{\Delta t} = -i \left[ \mathbf{H}_0 + \mathbf{F}^{n+1/2} \right] \mathbf{Y}^{n+1/2}, \quad (33)$$

where, the superscript  $n + 1/2$  represents the value at the mid-point time  $t_n + \Delta t/2$ . Making use of approximation

$$\mathbf{Y}^{n+1/2} \approx \frac{\mathbf{Y}^{n+1} + \mathbf{Y}^n}{2}, \quad (34)$$

Eq. (33) can be written as

$$\left( 1 - \mathbf{Q}^{n+1/2} \right) \mathbf{Y}^{n+1} = \left( 1 + \mathbf{Q}^{n+1/2} \right) \mathbf{Y}^n, \quad (35)$$

with

$$\mathbf{Q}^{n+1/2} = -\frac{i\Delta t}{2} \left[ \mathbf{H}_0 + \mathbf{F}^{n+1/2} \right]. \quad (36)$$

Since the coefficient matrix is sparse the algebraic equation (35) can be solved by using high-performance and memory efficient software packages. One of such kinds of packages is PARDISO, a package of parallel sparse direct and multi-recursive interactive linear solvers [22], which will be used in our calculations.

## IV. ABOVE-THRESHOLD IONIZATION AND PHOTOELECTRON ANGULAR DISTRIBUTION

To isolate the continuum-state wavefunction from the total wavefunction so as to calculate the ionization probability and photoelectron distribution, we introduce a bound-state projection operator  $\hat{P}_B$  and a continuum-state projection operator  $\hat{P}_C$ , respectively, by

$$\hat{P}_B = \sum_{\text{all } E_\alpha < 0} |\psi_\alpha\rangle \langle \psi_\alpha|, \quad (37)$$

and

$$\hat{P}_C = \sum_{\text{all } E_\alpha \geq 0} |\psi_\alpha\rangle \langle \psi_\alpha|, \quad (38)$$

where,  $E_\alpha$  and  $|\psi_\alpha(\mathbf{k})\rangle$  are the eigenvalue and eigenfunction of the unperturbed Hamiltonian  $\mathbf{H}_0$ . Obviously  $\hat{P}_B + \hat{P}_C = I$ . Using the projection operators, the bound-state wavefunction  $\varphi_B(\mathbf{k}, t)$  and continuum-state wavefunction  $\varphi_C(\mathbf{k}, t)$  can be calculated from the total wavefunction  $\varphi(\mathbf{k}, t)$  by

$$\varphi_B(\mathbf{k}, t) = \hat{P}_B \varphi(\mathbf{k}, t) = \sum_{\text{all } E_\alpha < 0} c_\alpha |\psi_\alpha(\mathbf{k})\rangle, \quad (39)$$

and

$$\varphi_C(\mathbf{k}, t) = \hat{P}_C \varphi(\mathbf{k}, t) = \sum_{\text{all } E_\alpha \geq 0} c_\alpha |\psi_\alpha(\mathbf{k})\rangle, \quad (40)$$

respectively. Here,  $c_\alpha = \langle \psi_\alpha(\mathbf{k}) | \varphi(\mathbf{k}, t) \rangle$  is the coefficient and  $|c_\alpha|^2$  is the probability on the unperturbed eigenstate  $\alpha$ .

The multiphoton ATI spectra and PADs can be calculated directly from the  $\mathcal{P}$ -space wavefunction [10]. At the end of the laser pulse ( $t = t_f$ ), the triple differential ionization probability density of a photoelectron having momentum  $\mathbf{k} = (k, \theta, \phi)$  is given by

$$\frac{dP(\mathbf{k})}{d\mathbf{k}} = \frac{\partial^3 P}{k^2 \partial k \partial \Omega} = |\varphi_C(\mathbf{k}, t_f)|^2, \quad (41)$$

where,  $d\mathbf{k} = k^2 dk d\Omega$ . The triple differential ionization probability density of a photoelectron having kinetic energy  $E = k^2/2$  and along direction  $\hat{\mathbf{k}} = (\theta, \phi)$  is computed from

$$\frac{\partial^3 P}{\partial E \partial \Omega} = k \frac{dP(\mathbf{k})}{d\mathbf{k}} = k |\varphi_C(\mathbf{k}, t_f)|^2. \quad (42)$$

The double differential ionization probability that describes the PADs is

$$\frac{d^2 P}{d\Omega} = \int |\varphi_C(\mathbf{k}, t_f)|^2 k^2 dk, \quad (43)$$

the differential ionization probability that characterizes the ATI spectra is given by

$$\frac{dP}{dE} = \int k |\varphi_C(\mathbf{k}, t_f)|^2 d\Omega, \quad (44)$$

and the total ionization probability is

$$P = \int |\varphi_C(\mathbf{k}, t_f)|^2 d\mathbf{k}. \quad (45)$$

## V. RESULTS AND DISCUSSION

The proposed approach has been applied to the study of multiphoton ATI of a hydrogen atom in superintense X-ray laser fields with  $\omega = 5.0$  a.u. ( $\lambda = 9.11$  nm) and  $\phi = 0$ . The maximum partial waves  $L_M$  and grid points  $N_M$  used in the calculation vary with the field strength and pulse duration. More partial waves and grid points are needed for higher-intensity and/or longer-pulse laser fields. In general, the converged ATI spectra and PADs are acquired when enough large values of  $L_M$  and  $N_M$  are employed. However, for the laser intensities and pulse durations considered here, particularly for  $E_0 = 50$  a.u. and  $T_P = 10$  OCs, the 3D nondipole calculations are still challenges to mid-size supercomputers when the same  $L_M$  and  $N_M$  are used in the computation of both ATI spectra and PADs. Fortunately, we find that the converged ATI spectra and PADs can be obtained, respectively, by using the different values of  $L_M$  and  $N_M$ .

To find suitable values of the pair  $(L_M, N_M)$  for converged calculations of ATI spectra and PADs, we have performed comprehensive computations using different values of  $(L_M, N_M)$ . In Figures 1 (a) to (d), the dipole ATI spectra are plotted for  $E_0 = 50$  a.u. and  $T_P = 10$  OCs. It is shown that the ATI spectra do not change much with  $L_M$  when  $L_M \geq 7$  for  $N_M \geq 1000$  (see figures 1 (a)-(c)) but vary greatly with  $N_M$  even for  $L_M = 9$  (see figure 1 (d)) when  $N_M < 1000$ . Thus the ATI spectra are more sensitive to  $N_M$  when  $N_M$  is less than some values and the converged ATI spectra can be obtained by using smaller  $L_M$  as long as  $N_M$  is large enough. In figures 1 (e) and (f), the dipole and nondipole ATI spectra are displayed, respectively, for  $E_0 = 15$  a.u. and  $T_P = 5$  OCs using different values of



$(L_M, N_M)$ . It is shown that the converged nondipole ATI spectra can be achieved when the same values of  $(L_M, N_M)$  are employed as those for the converged dipole calculations. Thus in the calculations of ATI spectra, the values of  $(L_M, N_M) = (5, 400)$  for  $E_0 = 10$  a.u. and  $T_P = 3$  OCs to  $(L_M, N_M) = (7, 1000)$  for  $E_0 = 50$  a.u. and  $T_P = 10$  OCs are employed.

In figure 2 the PADs obtained from the calculations using different values of  $(L_M, N_M)$  are plotted for  $E_0 = 50$  a.u. and  $T_P = 10$  OCs. Figures 2 (a)-(c) show that the dipole PAD obtained from the calculation with  $(L_M, N_M) = (10, 200)$  is very close to that with  $(L_M, N_M) = (10, 1200)$  and the PADs are insensitive to  $N_M$  when  $N_M \geq 200$  for  $L_M = 10$ . While figures 2 (d)-(f) show that the PAD with  $(L_M, N_M) = (5, 1000)$  is quite different from that with  $(L_M, N_M) = (9, 1000)$  and thus the PADs are more sensitive to  $L_M$  than to  $N_M$ . In figures 2 (g)-(l) the nondipole PADs are displayed. It is shown that the nondipole PADs are also insensitive to  $N_M$  but quite sensitive to  $L_M$ . From figures 2 (g) and (h) as well as figures 2 (i) and (j), for the same  $L_M$  the PAD using  $N_M = 200$  is very close to that using  $N_M = 300$ . Thus the PADs using  $N_M = 200$  is converged. From figures 2 (k) and (l), the PADs using  $(L_M, N_M) = (20, 200)$  and  $(L_M, N_M) = (23, 200)$  are very close to each other. Thus we employ  $(L_M, N_M) = (20, 200)$  in the calculations of PADs.

Using the parameters above, the ATI spectra and PADs of a hydrogen atom in superintense X-ray laser fields are computed using the nondipole  $\mathcal{P}$ -space approach for the laser field strengths  $E_0$  being 10, 30, and 50 a.u. and the laser pulse durations  $T_P$  being 3, 5, and 10 OCs. In Figure 3, the nondipole ATI spectra are plotted together with those of dipole approximation [10] for comparison. It is shown that in the shorter-pulse and lower-intensity laser fields the nondipole ATI spectra are almost identical with the dipole ones, as displayed in Figures 3 (a), (b), and (d). With the increase of laser intensity and/or pulse duration, the ATI spectra from the two approaches are gradually separated from each other. In the longer-pulse and/or higher-intensity laser fields, the nondipole ATI spectra are quite different from the dipole ones, as shown in Figures 3 (h) and (i). Compared to the dipole ATI spectra, the relative peak heights (the difference of the maxima and minima) of the nondipole ATI spectra are much smaller and thus the ATI peaks become less well resolved in the scales of the figures. Moreover, the nondipole ATI spectra are enhanced substantially in the high energy region, demonstrating the underestimation of the dipole approximation to the ionization probability of high energy electron.

To explore the mechanism for the enhancement of the ATI spectra in the high energy region, we study dipole and nondipole laser-electron interactions. From Eq. (2), the spatial dependence of the laser field  $\mathbf{A}(\mathbf{r}, t)$  comes from two parts that contain  $\mathbf{k}_L \cdot \mathbf{r}$  in the envelope factor  $\sin^2(\pi\eta/\omega T_P)$  and oscillation term  $\sin(\eta + \phi)$ . They are given by  $f_1 = (\pi/\omega T_P)(\mathbf{k}_L \cdot \mathbf{r})$  and  $f_2 = \mathbf{k}_L \cdot \mathbf{r}$ , respectively. For a laser field with pulse duration of  $N_{OC}$  OCs the ratio  $f_1/f_2 = \pi/\omega T_P = 1/2N_{OC}$  is negligibly small when  $N_{OC} \geq 3$ . In this case, the spatial dependence in the envelope factor can be fairly neglected compared to that in the oscillation term. Using Taylor series of sine function,  $\mathbf{A}(\mathbf{r}, t)$  can be well approximated by

$$\mathbf{A}(\mathbf{r}, t) \approx \mathbf{e}_x \frac{cE_0}{\omega} \sin^2\left(\frac{\pi t}{T_P}\right) \sum_{n=0}^{\infty} a_n (\mathbf{k}_L \cdot \mathbf{r})^n, \quad (46)$$

where,  $a_n = (-1)^n g_n(\omega t + \phi)/n!$  and  $g_n(x) = d^n \sin x / dx^n$ . On the RHS of Eq. (46), the first term with  $n = 0$  is the dipole term and all the others proportional to  $(\mathbf{k}_L \cdot \mathbf{r})^n$  with  $n > 0$  are nondipole terms. The dipole term is inversely proportional to  $\omega$  (proportional to  $\lambda$ ) and independent of  $\mathbf{k}_L \cdot \mathbf{r}$ , while the nondipole interaction terms are proportional to  $\mathbf{k}_L \cdot \mathbf{r}$  and  $\omega$  (inversely proportional to  $\lambda$ ) except the term with  $n = 1$  which is independent of  $\omega$  (and  $\lambda$ ). In shorter-wavelength (higher-frequency) and/or higher-intensity and/or longer-pulse laser fields, the nondipole interaction terms  $(\mathbf{k}_L \cdot \mathbf{r})^n$  may not be much smaller than the dipole interaction term, particularly for the processes involving ionization where the photoelectron may go to the place very far from the nucleus. Thus the dipole approximation is a good approach only for longer-wavelength, lower-intensity, and short-pulse laser fields. The laser-electron interaction is proportional to  $\mathbf{A} \cdot \mathbf{k}$  and increases with the photoelectron momentum  $k$ . Thus in the nondipole approach the effect of the nondipole interactions is mainly on the photoelectron with large  $k$ , making the ATI spectra enhanced significantly in the high energy region. In addition, in longer-pulse laser fields the photoelectron can achieve more energy and thus the enhancement of the ATI spectra can be more easily observed.

In Figure 4, the PADs of dipole approximation [10] are plotted. It is shown that the PADs consist of two lobes for the laser fields considered and are cylindrically symmetric with respect to the laser polarization direction. In the lower-intensity laser fields, the left lobes are almost the same as the right lobes, the PADs do not change apparently with pulse duration, and the interfaces between the two lobes are very small, as shown in figures 4 (a), (d), and (g). In contrast, in the higher-intensity laser fields, the PADs change significantly with the pulse duration and the interfaces between the two lobes become large. For the shorter-pulse laser fields, the laser fields along the polarization direction are quite different from those against the polarization direction and thus the left lobes are different from the right lobes, as displayed in figures 4 (b) and (c). However, for the longer-pulse laser fields, the laser fields along the polarization direction are very close to those against the polarization direction and thus the left and right lobes are almost the same, as shown in figures 4 (h) and (i).

In Figure 5, the PADs from the nondipole calculations are displayed. It is shown that in the lower-intensity laser fields the nondipole PADs shown in figures 5 (a), (d), and (g) are composed of two lobes and are very close to the corresponding dipole counterparts in figures 4 (a), (d), and (g). With the increase of laser intensity, the nondipole PADs are getting different from the dipole ones. In the higher-intensity laser fields, with the increase of the pulse duration, the distortions of the PADs become larger. Particularly two additional lobes are induced along and against the laser propagation direction, respectively, as shown in Figure 5 (c), (f), and (i). This is different from the result of a hydrogen atom in XUV laser fields, where only one lobe against the laser propagation direction is predicted [11, 12].

To probe the mechanism of the distortion in nondipole PADs, we investigate the laser-electron interaction change with electron positions. From Eq. (46), the dipole term is independent of  $r \cos \theta$  but decreases with  $\omega$ . The nondipole terms depend on  $r \cos \theta$  and increase with  $\omega$  except the term with  $n = 1$  which is independent of  $\omega$ . The nondipole interaction for the electron far from the nucleus is larger than that for the electron close to the nucleus. Due to the dependence of  $\cos \theta$  the nondipole interaction is anisotropic and largest in the directions of  $\theta = 0$  and  $\pi$ . Thus the nondipole PADs along and against the laser propagation direction are much easier to distort than other directions and the cylindrical symmetry with respect to the laser polarization direction in the dipole PADs is destroyed in the nondipole PADs.

## VI. SUMMARY AND CONCLUSION

In summary, we have proposed an accurate and efficient nondipole computational approach in  $\mathcal{P}$  space for the study of multiphoton ATI of atoms in the presence of superintense ultrashort-wavelength laser fields. This approach has been applied to the calculation of ATI spectra and PADs of a hydrogen atom exposed to the superintense X-ray laser fields. It is shown that the nondipole ATI spectra and PADs are very close to the dipole ones in the lower-intensity and shorter-pulse laser fields. With the increase of the laser intensity and/or laser pulse duration, the nondipole results are getting different from the dipole ones. In the higher-intensity and/or longer-pulse laser fields, the nondipole ATI peaks become less well resolved and the ATI spectra are enhanced substantially in the high energy region. The nondipole PADs are significantly distorted along and against the laser propagation direction and the cylindrical symmetry with respect to the laser polarization direction in the dipole PADs is destroyed in the nondipole PADs. To explore the mechanisms of the substantial enhancement of the ATI spectra and the significant distortion of the PADs, we have investigated the laser-electron interaction analytically, particularly the nondipole laser-electron interaction terms change with the momentum and direction of the photoelectron. We find that the nondipole laser-electron interaction terms are anisotropic and increases with the photoelectron momentum. The enhancement of the multiphoton ATI spectra in the high energy region can be attributed directly to the fact that the nondipole laser-electron interactions increase with the photoelectron momentum, while the distortions of the PADs along and against the laser propagation directions can be attributed to the fact that the nondipole laser-electron interactions are anisotropic. Thus for the nonperturbative study of multiphoton ionization processes in the superintense longer-pulse ultrashort-wavelength laser fields the dipole approximation is no longer a good approach and instead the nondipole approach should be used. Since the nondipole interactions depend on the position of electron, the validity of the dipole approximation is not only decided by the laser wavelength (frequency) but also by the laser intensity and duration.

It is desirable to compare the  $\mathcal{P}$ -space nondipole approach proposed in this paper with other approaches. The distinctions between the  $\mathcal{P}$ -space nondipole approach and the  $\mathcal{P}$ -space dipole approximation developed in [10] are summarized below. (1) The theoretical frameworks are different. The  $\mathcal{P}$ -space nondipole computational approach is based on the nondipole approach, while the  $\mathcal{P}$ -space dipole approach is based on the dipole approximation. (2) The  $\mathcal{P}$ -space dipole approximation can only be applied to the longer-wavelength, lower-intensity, and shorter-pulse laser fields, while the  $\mathcal{P}$ -space nondipole approach can, in principle, be applied to the higher-intensity and/or shorter-wavelength (e.g., X-ray) as well as longer-pulse laser fields. (3) The numerical methods are different. In the  $\mathcal{P}$ -space dipole approximation, the calculations are 2-dimensional and the split-operator method is used to propagate the wavefunction. In the  $\mathcal{P}$ -space nondipole approach, due to the spatial dependence of the nondipole components of the laser fields, the calculations are 3-dimensional even for the hydrogen atom, making the computation quite difficult. To conquer this difficulty, the symplectic algorithm is extended to discretize the  $\mathcal{P}$ -space TDSE. Since the coefficient matrix in the TD matrix equation is sparse, the parallel high-performance and memory efficient software packages for sparse matrixes can be used to propagate the wavefunction. (4) The results from the two approaches are different. It is very clearly shown in Figures 3~5 that both the ATI spectra and PADs of the  $\mathcal{P}$ -space nondipole calculations are quite different from those of the  $\mathcal{P}$ -space dipole calculations in the higher-intensity and/or longer-pulse laser fields.

The differences between the  $\mathcal{P}$ -space nondipole approach and the  $\mathcal{R}$ -space nondipole approach recently presented in [11, 12] are outlined below. (1) The  $\mathcal{R}$ -space nondipole approach is developed in the Kramers-Henneberger frame. In this approach, some higher-order nondipole interaction terms are neglected. The  $\mathcal{P}$ -space nondipole approach is proposed in the  $\mathcal{P}$  space. In this approach, all the nondipole interaction terms are taken into account. (2) In the

$\mathcal{R}$ -space nondipole approach the electron wavefunction is calculated by solving the TDSE in the  $\mathcal{R}$  space, while in the  $\mathcal{P}$ -space nondipole approach the electron wavefunction is computed by solving the TDSE in the  $\mathcal{P}$  space. Compared to the  $\mathcal{R}$ -space nondipole approach, the  $\mathcal{P}$ -space nondipole approach has four advantages. (1) More accurate. The  $\mathcal{P}$ -space approach is based on the fact that the momentum of an electron in any physics process is always finite and less than a certain maximum value. Thus the wavefunction can be more accurately calculated with a simple zero boundary condition within a finite  $\mathcal{P}$  space without any reflection on the boundary. (2) More efficient. After discretization using the symplectic algorithm the Hamiltonian matrix in the  $\mathcal{P}$ -space approach is sparse. Thus the wavefunction can be more efficiently propagated using the parallel high-performance and memory efficient software packages. (3) The  $\mathcal{P}$ -space approach includes all the nondipole interaction terms and thus can be applied to the study of atoms in superintense and ultrashort-wavelength (X-ray) laser fields where the higher-order nondipole interaction terms become more significant. (4) More elaborate structures can be obtained when the  $\mathcal{P}$ -space approach is applied to the study of multiphoton ATI spectra and PADs of a hydrogen atom exposed to superintense X-ray laser fields. In higher-intensity and/or longer-pulse laser fields, the multiphoton ATI spectra from the  $\mathcal{P}$ -space nondipole approach are enhanced substantially in the high energy regime compared to those from the  $\mathcal{P}$ -space dipole approximation. The PADs from the  $\mathcal{P}$ -space nondipole approach are distorted significantly in the higher-intensity and/or longer-pulse laser fields. In particular, two additional lobes are induced along and against the laser propagation directions, respectively, which is quite different from the PADs of the  $\mathcal{R}$ -space nondipole approach, where only one lobe against the laser propagation direction is predicted [11, 12].

### Appendix A: $\mathcal{P}$ -space laser-electron interactions

Substituting Eq. (2) into Eqs. (9) and (10), we obtain

$$D(\mathbf{k}, \mathbf{k}', t) = \frac{iE_0}{16\omega} \mathbf{e}_x \cdot (\mathbf{k} + \mathbf{k}') \left[ -2e^{i\beta} \delta(\mathbf{k}' - \mathbf{k} - \mathbf{k}_L) + 2e^{-i\beta} \delta(\mathbf{k}' - \mathbf{k} + \mathbf{k}_L) \right. \\ \left. + e^{i\beta_3} \delta(\mathbf{k}' - \mathbf{k} - \mathbf{k}_{L3}) - e^{-i\beta_3} \delta(\mathbf{k}' - \mathbf{k} + \mathbf{k}_{L3}) \right. \\ \left. + e^{i\beta_4} \delta(\mathbf{k}' - \mathbf{k} - \mathbf{k}_{L4}) - e^{-i\beta_4} \delta(\mathbf{k}' - \mathbf{k} + \mathbf{k}_{L4}) \right], \quad (\text{A1})$$

and

$$B(\mathbf{k}, \mathbf{k}', t) = -\frac{E_0^2}{128\omega^2} \left[ 8e^{i2\beta_0} \delta(\mathbf{k}' - \mathbf{k} - 2\mathbf{k}_{L0}) + 8e^{-i2\beta_0} \delta(\mathbf{k}' - \mathbf{k} + 2\mathbf{k}_{L0}) \right. \\ - 2e^{i4\beta_0} \delta(\mathbf{k}' - \mathbf{k} - 4\mathbf{k}_{L0}) - 2e^{-i4\beta_0} \delta(\mathbf{k}' - \mathbf{k} + 4\mathbf{k}_{L0}) \\ + 6e^{i2\beta} \delta(\mathbf{k}' - \mathbf{k} - 2\mathbf{k}_L) + 6e^{-i2\beta} \delta(\mathbf{k}' - \mathbf{k} + 2\mathbf{k}_L) \\ - 4e^{i2\beta_1} \delta(\mathbf{k}' - \mathbf{k} - 2\mathbf{k}_{L1}) - 4e^{-i2\beta_1} \delta(\mathbf{k}' - \mathbf{k} + 2\mathbf{k}_{L1}) \\ - 4e^{i2\beta_2} \delta(\mathbf{k}' - \mathbf{k} - 2\mathbf{k}_{L2}) - 4e^{-i2\beta_2} \delta(\mathbf{k}' - \mathbf{k} + 2\mathbf{k}_{L2}) \\ + e^{i2\beta_3} \delta(\mathbf{k}' - \mathbf{k} - 2\mathbf{k}_{L3}) + e^{-i2\beta_3} \delta(\mathbf{k}' - \mathbf{k} + 2\mathbf{k}_{L3}) \\ + e^{i2\beta_4} \delta(\mathbf{k}' - \mathbf{k} - 2\mathbf{k}_{L4}) + e^{-i2\beta_4} \delta(\mathbf{k}' - \mathbf{k} + 2\mathbf{k}_{L4}) \\ \left. - 12\delta(\mathbf{k}' - \mathbf{k}) \right], \quad (\text{A2})$$

where,  $a_0 = \pi/\omega T_P$ ,  $\mathbf{k}_{L0} = a_0 \mathbf{k}_L$ ,  $\mathbf{k}_{L1} = (1 + a_0) \mathbf{k}_L$ ,  $\mathbf{k}_{L2} = (1 - a_0) \mathbf{k}_L$ ,  $\mathbf{k}_{L3} = (1 + 2a_0) \mathbf{k}_L$ ,  $\mathbf{k}_{L4} = (1 - 2a_0) \mathbf{k}_L$ ,  $\beta(t) = \omega t + \phi$ ,  $\beta_0(t) = a_0 \omega t$ ,  $\beta_1(t) = (1 + a_0) \omega t + \phi$ ,  $\beta_2(t) = (1 - a_0) \omega t + \phi$ ,  $\beta_3(t) = (1 + 2a_0) \omega t + \phi$ , and  $\beta_4(t) = (1 - 2a_0) \omega t + \phi$ . It is easy to verify that  $D^\dagger(\mathbf{k}', \mathbf{k}, t) = D(\mathbf{k}, \mathbf{k}', t)$  and  $B^\dagger(\mathbf{k}', \mathbf{k}, t) = B(\mathbf{k}, \mathbf{k}', t)$ . Thus the  $\mathcal{P}$ -space Hamiltonian in Eq. (7),  $H(\mathbf{k}, \mathbf{k}', t)$ , is Hermitian.

### Appendix B: $\mathcal{P}$ -space partial wave laser-electron interactions

Substitute Eqs. (A1) and (A2) into Eqs. (17) and (18), respectively, we obtain

$$D_{lm, l'm'}(k, k', t) = -\frac{E_0 i}{16\omega} \left\{ 2 \left[ e^{i\beta} \lambda_{lm, l'm'}(k, k', k_L) - e^{-i\beta} \lambda_{lm, l'm'}^\dagger(k, k', k_L) \right] \right. \\ \left. - \left[ e^{i\beta_3} \lambda_{lm, l'm'}(k, k', k_{L3}) - e^{-i\beta_3} \lambda_{lm, l'm'}^\dagger(k, k', k_{L3}) \right] \right. \\ \left. - \left[ e^{i\beta_4} \lambda_{lm, l'm'}(k, k', k_{L4}) - e^{-i\beta_4} \lambda_{lm, l'm'}^\dagger(k, k', k_{L4}) \right] \right\}, \quad (\text{B1})$$

and

$$\begin{aligned}
B_{lm,l'm'}(k,k',t) = & -\frac{E_0^2}{128\omega^2} \left\{ 8 \left[ e^{i2\beta_0} \eta_{lm,l'm'}(k,k',2k_{L0}) + e^{-i2\beta_0} \eta_{lm,l'm'}^\dagger(k,k',2k_{L0}) \right] \right. \\
& -2 \left[ e^{i4\beta_0} \eta_{lm,l'm'}(k,k',4k_{L0}) + e^{-i4\beta_0} \eta_{lm,l'm'}^\dagger(k,k',4k_{L0}) \right] \\
& +6 \left[ e^{i2\beta} \eta_{lm,l'm'}(k,k',2k_L) + e^{-i2\beta} \eta_{lm,l'm'}^\dagger(k,k',2k_L) \right] \\
& -4 \left[ e^{i2\beta_1} \eta_{lm,l'm'}(k,k',2k_{L1}) + e^{-i2\beta_1} \eta_{lm,l'm'}^\dagger(k,k',2k_{L1}) \right] \\
& -4 \left[ e^{i2\beta_2} \eta_{lm,l'm'}(k,k',2k_{L2}) + e^{-i2\beta_2} \eta_{lm,l'm'}^\dagger(k,k',2k_{L2}) \right] \\
& + \left[ e^{i2\beta_3} \eta_{lm,l'm'}(k,k',2k_{L3}) + e^{-i2\beta_3} \eta_{lm,l'm'}^\dagger(k,k',2k_{L3}) \right] \\
& + \left[ e^{i2\beta_4} \eta_{lm,l'm'}(k,k',2k_{L4}) + e^{-i2\beta_4} \eta_{lm,l'm'}^\dagger(k,k',2k_{L4}) \right] \\
& \left. -12 \frac{k}{k'} \delta(k' - k) \delta_{ll'} \delta_{mm'} \right\}, \tag{B2}
\end{aligned}$$

where,

$$\begin{aligned}
\lambda_{lm,l'm'}(k,k',K) = & kk' \int \int Y_{lm}^*(\theta, \phi) (k_x + k'_x) \delta(\mathbf{k}' - \mathbf{k} - \mathbf{K}) Y_{l'm'}(\theta', \phi') d\Omega d\Omega' \\
= & \frac{1}{4} k \sqrt{\frac{(2l+1) \Gamma(l-m+1) \Gamma(l'-m'+1)}{(2l'+1) \Gamma(l+m+1) \Gamma(l'+m'+1)}} \\
& \times \{ \delta_{mm'+1} [\zeta_{lm,l'-1m'+1}(k,k',K) - \zeta_{lm,l'+1m'+1}(k,k',K) \\
& + \frac{(2l'+1)k}{(2l+1)k'} ((l-m+2)(l-m+1)\zeta_{l+1m-1,l'm'}(k,k',K) \\
& - (l+m)(l+m-1)\zeta_{l-1m-1,l'm'}(k,k',K))] \\
& + \delta_{mm'-1} \left[ \frac{(2l'+1)k}{(2l+1)k'} (\zeta_{l-1m+1,l'm'}(k,k',K) - \zeta_{l+1m+1,l'm'}(k,k',K)) \right. \\
& \left. + (l'-m'+2)(l'-m'+1)\zeta_{lm,l'+1m'-1}(k,k',K) \right. \\
& \left. - (l'+m')(l'+m'-1)\zeta_{lm,l'-1m'-1}(k,k',K) \right] \}, \tag{B3}
\end{aligned}$$

$$\begin{aligned}
\eta_{lm,l'm'}(k,k',K) = & kk' \int \int Y_{lm}^*(\theta, \phi) \delta(\mathbf{k}' - \mathbf{k} - \mathbf{K}) Y_{l'm'}(\theta', \phi') d\Omega d\Omega' \\
= & \frac{1}{2} \frac{k}{k'} \sqrt{(2l+1)(2l'+1) \frac{\Gamma(l-m+1) \Gamma(l'-m'+1)}{\Gamma(l+m+1) \Gamma(l'+m'+1)}} \zeta_{lm,l'm'}(k,k',K) \delta_{mm'}, \tag{B4}
\end{aligned}$$

and

$$\zeta_{lm,l'm'}(k,k',K) = \int P_l^m(\cos\theta) \delta(k' - q) P_{l'}^{m'}(\cos\theta_q) d\cos\theta. \tag{B5}$$

Here,  $\eta_{lm,l'm'}^\dagger(k,k',K)$  and  $\lambda_{lm,l'm'}^\dagger(k,k',K)$  are the conjugate transpose of  $\eta_{lm,l'm'}(k,k',K)$  and  $\lambda_{lm,l'm'}(k,k',K)$ , respectively, and  $P_l^m(\cos\theta)$  is the associated Legendre function. If  $\mathbf{K}$  is a vector along  $z$  axis and  $\mathbf{k}$  is a vector arbitrarily oriented, the spherical coordinates  $(q, \theta_q, \phi_q)$  of a vector  $\mathbf{q} = \mathbf{k} + \mathbf{K}$  are computed by

$$\begin{cases} q = \sqrt{k^2 + 2kK \cos\theta + K^2} \\ \theta_q = \tan^{-1} \left( \frac{k \sin\theta}{k \cos\theta + K} \right) \\ \phi_q = \phi \end{cases}, \tag{B6}$$

where,  $K = |\mathbf{K}|$  and  $(k, \theta, \phi)$  are the spherical coordinates of the vector  $\mathbf{k}$ .

From Eqs. (B1) to (B4),  $D_{lm,l'm'}(k,k',t) \neq 0$  when and only when  $m' = m \pm 1$  and  $B_{lm,l'm'}(k,k',t) \neq 0$  when and only when  $m' = m$ . Thus  $D(t) = \{D_{lm,l'm'}(k,k',t)\}$  and  $B(t) = \{B_{lm,l'm'}(k,k',t)\}$  are sparse matrixes. It is easy to verify that when  $\mathbf{k}_L = 0$  the nondipole approach is degraded to the dipole approximation [10].

## Acknowledgments

This work was partially supported by the Chemical Sciences, Geosciences, and Biosciences Division of the Office of Basic Energy Sciences, Office of Sciences, U.S. Department of Energy and by the U.S. National Science Foundation. We would like to acknowledge also the partial support of National Science Council of Taiwan (Grant No. 97-2112-M-002-003-MY3) and National Taiwan University (Grants No. 98R0045 and No. 99R80870).

- 
- [1] J. Feldhaus, J. Arthur, and J. B. Hastings, *J. Phys. B: At. Mol. Opt. Phys.* **38**, S799 (2005).
  - [2] W. Ackermann, G. Asova, V. Ayvazyan, A. Azima, N. Baboi, J. Bähr, V. Balandin, B. Beutner, A. Brandt, A. Bolzmann, R. Brinkmann, O. I. Brovko, M. Castellano, P. Castro, L. Catani, E. Chiadroni, S. Choroba, A. Cianchi, J.T. Costello, D. Cubaynes, J. Dardis, W. Decking, H. Delsim-Hashemi, A. Delserieys, G. Di Pirro, M. Dohlus, S. Düsterer, A. Eckhardt, H. T. Edwards, B. Faatz, J. Feldhaus, K. Flöttmann, J. Frisch, L. Fröhlich, T. Garvey, U. Gensch, Ch. Gerth, M. Görler, N. Golubeva, H.-J. Grabosch, M. Grecki, O. Grimm, K. Hacker, U. Hahn, J. H. Han, K. Honkavaara, T. Hott, M. Hüning, Y. Ivanisenko, E. Jaeschke, W. Jalmuzna, T. Jezynski, R. Kammering, V. Katalev, K. Kavanagh, E. T. Kennedy, S. Khodyachykh, K. Klose, V. Kocharyan, M. Körfer, M. Kollwe, W. Koprek, S. Korepanov, D. Kostin, M. Krassilnikov, G. Kube, M. Kuhlmann, C. L. S. Lewis, L. Lilje, T. Limberg, D. Lipka, F. Löhler, H. Luna, M. Luong, M. Martins, M. Meyer, P. Michelato, V. Miltchev, W. D. Möller, L. Monaco, W. F. O. Müller, O. Napieralski, O. Napoly, P. Nicolosi, D. Nölle, T. Nuñez, A. Oppelt, C. Pagani, R. Paparella, N. Pchalek, J. Pedregosa-Gutierrez, B. Petersen, B. Petrosyan, G. Petrosyan, L. Petrosyan, J. Pflüger, E. Plönjes, L. Poletto, K. Pozniak, E. Prat, D. Proch, P. Pucyk, P. Radcliffe, H. Redlin, K. Rehlich, M. Richter, M. Roehrs, J. Roensch, R. Romaniuk, M. Ross, J. Rossbach, V. Rybnikov, M. Sachwitz, E. L. Saldin, W. Sandner, H. Schlarb, B. Schmidt, M. Schmitz, P. Schmüser, J. R. Schneider, E. A. Schneidmiller, S. Schnepf, S. Schreiber, M. Seidel, D. Sertore, A. V. Shabunov, C. Simon, S. Simrock, E. Sombrowski, A. A. Sorokin, P. Spanknebel, R. Spesyvtsev, L. Staykov, B. Steffen, F. Stephan, F. Stulle, H. Thom, K. Tiedtke, M. Tischer, S. Toleikis, R. Treusch, D. Trines, I. Tsakov, E. Vogel, T. Weiland, H. Weise, M. Wellhöfer, M. Wendt, I. Will, A. Winter, K. Wittenburg, W. Wurth, P. Yeates, M. V. Yurkov, I. Zagorodnov, and K. Zapfe, *Nat. Photon.*, **1**, 336 (2007).
  - [3] C. Gutt, L.-M. Stadler, S. Streit-Nierobisch, A. P. Mancuso, A. Schropp, B. Pfau, C. M. Günther, R. Könnecke, J. Gulden, B. Reime, J. Feldhaus, E. Weckert, I. A. Vartanyants, O. Hellwig, F. Staier, R. Barth, M. Grunze, A. Rosenhahn, D. Stickler, H. Stillrich, R. Frömter, H. P. Oepen, M. Martins, T. Nisius, T. Wilhein, B. Faatz, N. Guerassimova, K. Honkavaara, V. Kocharyan, R. Treusch, E. Saldin, S. Schreiber, E. A. Schneidmiller, M. V. Yurkov, S. Eisebitt, and G. Grübel, *Phys. Rev. B* **79**, 212406 (2009).
  - [4] M. Hoener, L. Fang, O. Kornilov, O. Gessner, S. T. Pratt, M. Gühr, E. P. Kanter, C. Blaga, C. Bostedt, J. D. Bozek, P. H. Bucksbaum, C. Buth, M. Chen, R. Coffee, J. Cryan, L. DiMauro, M. Glowina, E. Hosler, E. Kukk, S. R. Leone, B. McFarland, M. Messerschmidt, B. Murphy, V. Petrovic, D. Rolles, and N. Berrah, *Phys. Rev. Lett.* **104**, 253002 (2010).
  - [5] L. Fang, M. Hoener, O. Gessner, F. Tarantelli, S. T. Pratt, O. Kornilov, C. Buth, M. Gühr, E. P. Kanter, C. Bostedt, J. D. Bozek, P. H. Bucksbaum, M. Chen, R. Coffee, J. Cryan, M. Glowina, E. Kukk, S. R. Leone, and N. Berrah, *Phys. Rev. Lett.* **105**, 083005 (2010).
  - [6] J. P. Cryan, J. M. Glowina, J. Andreasson, A. Belkacem, N. Berrah, C. I. Blaga, C. Bostedt, J. Bozek, C. Buth, L. F. DiMauro, L. Fang, O. Gessner, M. Guehr, J. Hajdu, M. P. Hertlein, M. Hoener, O. Kornilov, J. P. Marangos, A. M. March, B. K. McFarland, H. Merdji, V. S. Petrović, C. Raman, D. Ray, D. Reis, F. Tarantelli, M. Trigo, J. L. White, W. White, L. Young, P. H. Bucksbaum, and R. N. Coffee, *Phys. Rev. Lett.* **105**, 083004 (2010).
  - [7] W. Li, R. R. Lucchese, A. Doyuran, Z. Wu, H. Loos, G. E. Hall, and A. G. Suits, *Phys. Rev. Lett.* **92**, 083002 (2004).
  - [8] N. Rohringer and R. Santra, *Phys. Rev. A* **76**, 033416 (2007).
  - [9] A. A. Sorokin, S. V. Bobashev, K. Tiedtke, and M. Richter, *J. Phys. B: At. Mol. Opt. Phys.* **39**, L299 (2006).
  - [10] Z. Zhou and S. I. Chu, *Phys. Rev. A* **83**, 013405 (2011).
  - [11] M. Førre, S. Selstø, J. P. Hansen, and L. B. Madsen, *Phys. Rev. Lett.* **95**, 043601 (2005).
  - [12] M. Førre, J. P. Hansen, L. Kocbach, S. Selstø, and L. B. Madsen, *Phys. Rev. Lett.* **97**, 043601 (2006).
  - [13] M. Førre, *Phys. Rev. A* **74**, 065401 (2006).
  - [14] M. Førre, S. Selstø, J. P. Hansen, T. K. Kjeldsen, and L. B. Madsen, *Phys. Rev. A* **76**, 033415 (2007).
  - [15] R. H. Landau, *Phys. Rev. C* **27**, 2191 (1983).
  - [16] K. M. Maung, D. E. Kahana, and J. W. Norbury, *Phys. Rev. D* **47**, 1182 (1993).
  - [17] Y. R. Kwon and F. Tabakin, *Phys. Rev. C* **18**, 932 (1978).
  - [18] I. A. Ivanov and J. Mitroy, *Comp. Phys. Commun.* **134**, 317 (2001).
  - [19] X. M. Tong and S. I. Chu, *Chem. Phys.* **217**, 119 (1997).
  - [20] Z. Zhou and S. I. Chu, *Phys. Rev. A* **71**, 022513 (2005).
  - [21] Z. Zhou, P. Ding, and S. Pan, *J. Korean Phys. Soc.* **32**, 417 (1998).
  - [22] *Intel Math Kernel Library*, Document Number: 630813-031US, <http://www.intel.com> (2009).

### Figure Captions

Figure 1: (Color online) ATI spectra for different  $L_M$  and  $N_M$ : (a)-(d) the dipole ATI spectra for  $E_0 = 50$  a.u. and  $T_P = 10$  OCs, (e) the dipole and (f) the nondipole ATI spectra for  $E_0 = 15$  a.u. and  $T_P = 5$  OCs.

Figure 2: (Color online) PADs for different  $L_M$  and  $N_M$ : (a)-(f) the dipole and (g)-(l) the nondipole PADs for  $E_0 = 50$  a.u. and  $T_P = 10$  OCs.

Figure 3: (Color online) Dipole (blue dashed curves) and nondipole (red solid curves) ATI spectra of a hydrogen atom in the X-ray laser fields with different laser intensities and pulse durations.

Figure 4: (Color online) Dipole PADs in the X-ray laser fields with different laser intensities and pulse durations. The laser field is along the horizontal direction and the laser propagation is along the vertical direction.

Figure 5: (Color online) Same as Figure 4 but for the nondipole PADs.

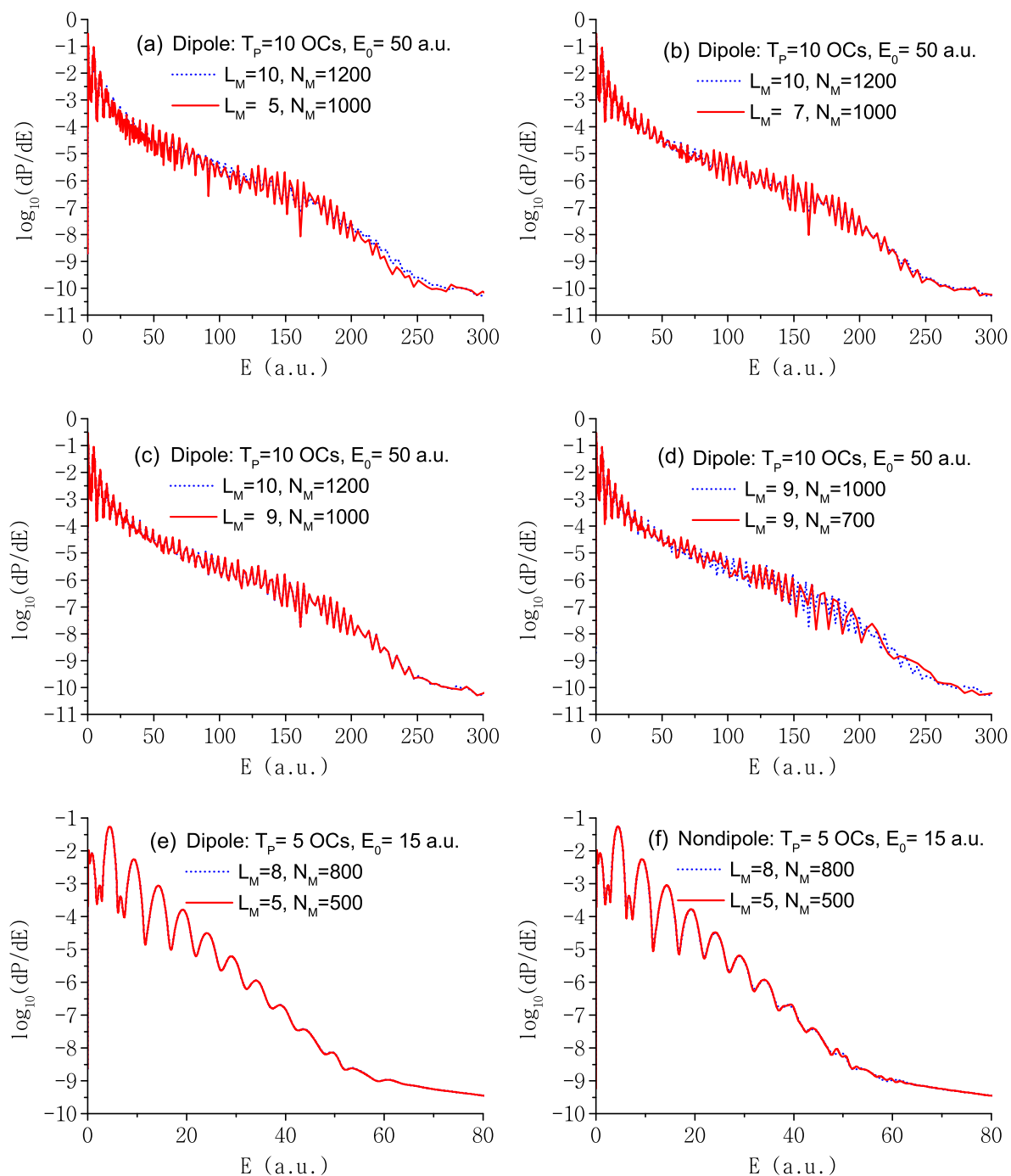


Figure 1

XXXXXXXXXX

29Jan2013

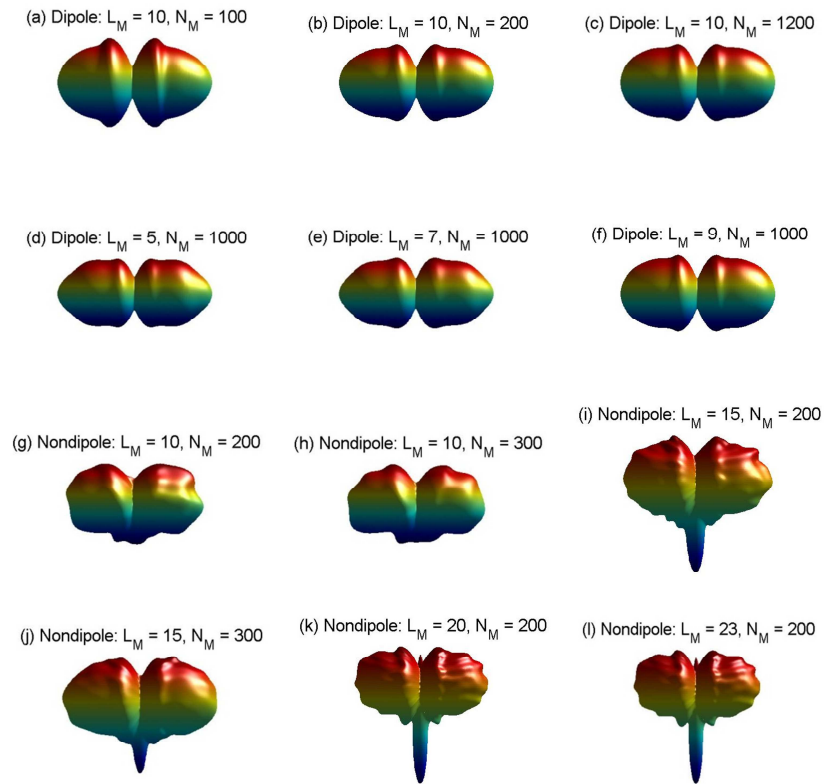


Figure 2

XXXXXXXXXX

29Jan2013



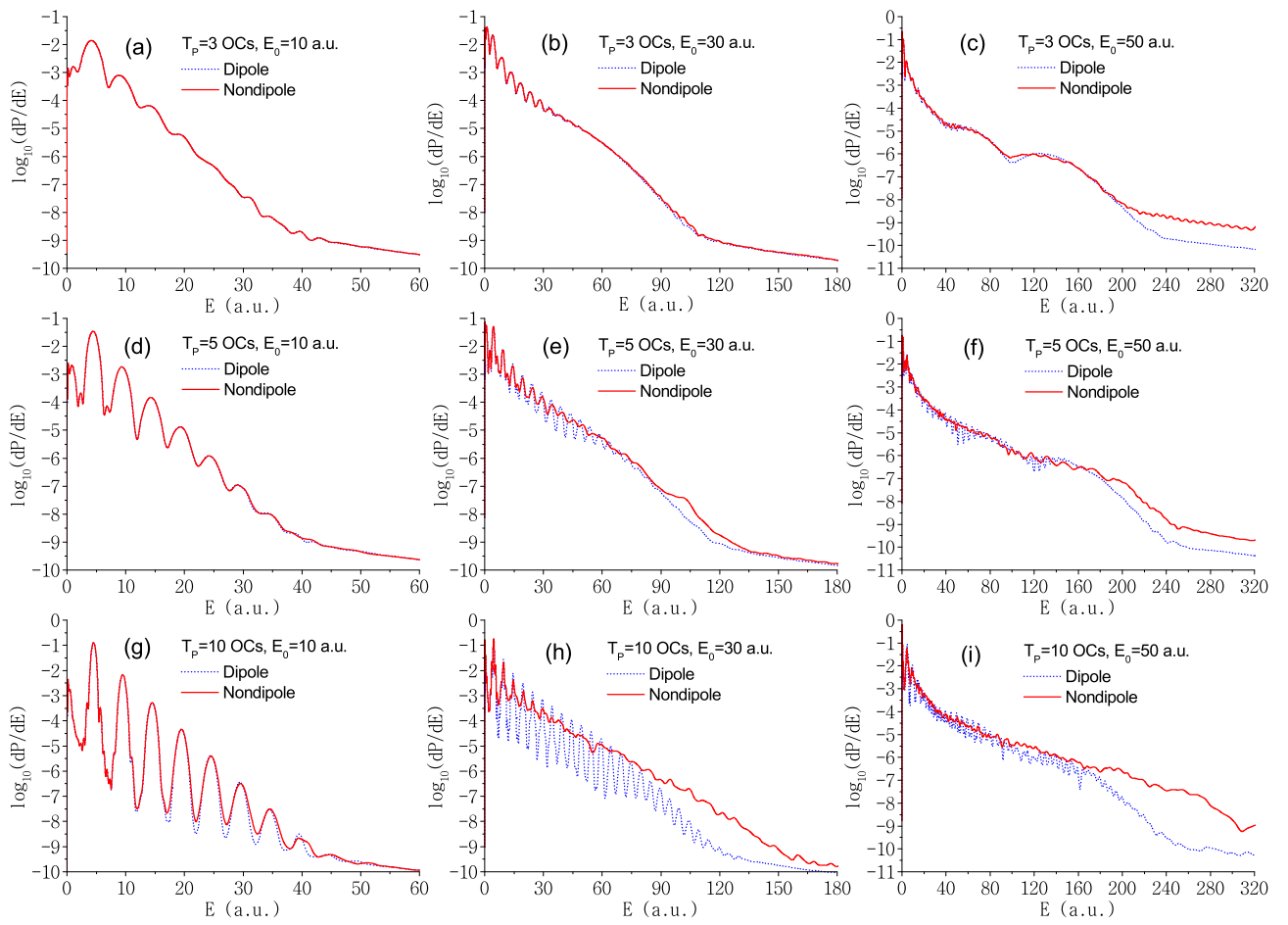
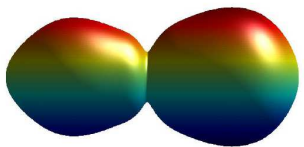


Figure 3

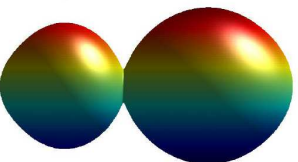
XXXXXXXXXX

29Jan2013

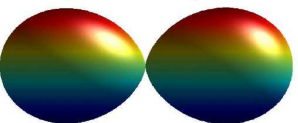
(c)  $T_P = 3$  OCs,  $E_0 = 50$  a.u.



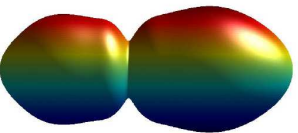
(b)  $T_P = 3$  OCs,  $E_0 = 30$  a.u.



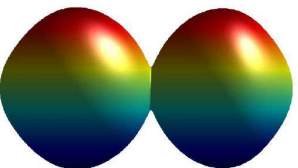
(a)  $T_P = 3$  OCs,  $E_0 = 10$  a.u.



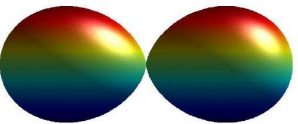
(f)  $T_P = 5$  OCs,  $E_0 = 50$  a.u.



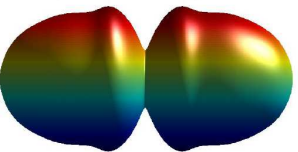
(e)  $T_P = 5$  OCs,  $E_0 = 30$  a.u.



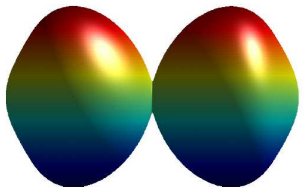
(d)  $T_P = 5$  OCs,  $E_0 = 10$  a.u.



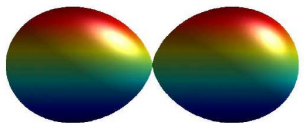
(i)  $T_P = 10$  OCs,  $E_0 = 50$  a.u.



(h)  $T_P = 10$  OCs,  $E_0 = 30$  a.u.



(g)  $T_P = 10$  OCs,  $E_0 = 10$  a.u.



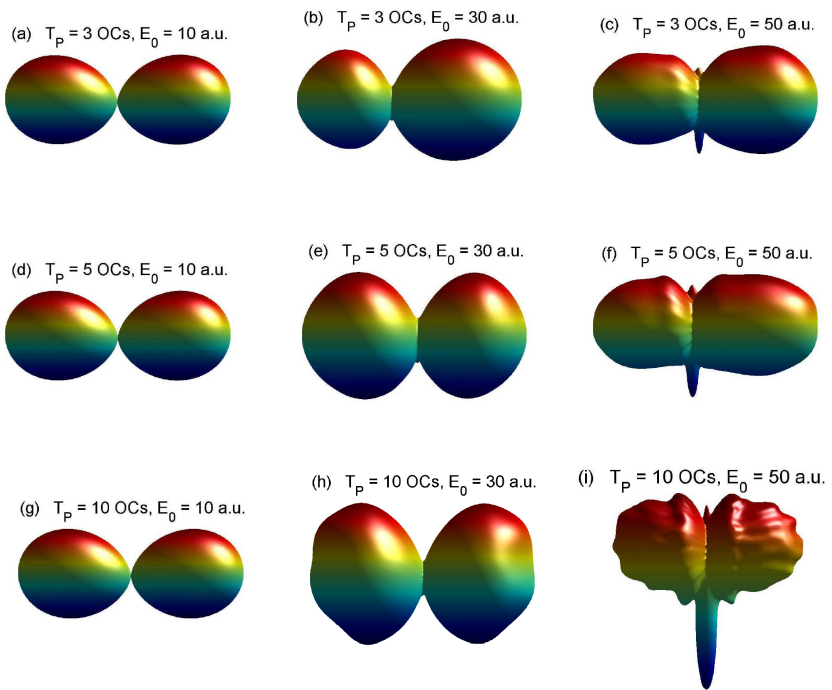


Figure 5

XXXXXXXXXX

29Jan2013